accelerated the reaction. Accordingly, acid catalysis through hydrogen bonding to the phenols or the glycoluril functions can be excluded as the source of acceleration. Although some form of acid catalysis might operate within the special microenvironment presented by the capsule to guests, this possibility remains untested, and may even be untestable. Finally, the corresponding reaction of 1,4 naphthoquinone **11**, a molecule too large for the capsule, was not accelerated by **1-1**. The factors of size selectivity, saturation kinetics, and product inhibition all support an encapsulated transition state.

The transition-state geometry of this reaction leading to the *endo* product is reminiscent, in size and shape, of two encapsulated benzene molecules oriented in a face-to-face stacking interaction. Accordingly, the acceleration of the Diels–Alder reaction inside the capsule is not unreasonable. Acceleration of the reverse of the Diels–Alder reaction by encapsulation is unreasonable, and we interpret the accelerating effect of encapsulation on the forward rate as resulting from an enhanced concentration of the reactants inside the capsule, rather than some special stabiization of the transition state. Using a technique described elsewhere[10], we estimate the interior volume of the capsule to be ~300 Å^3. When this space is occupied with one molecule of quinone and cyclohexadiene, the concentration of each reactant inside the capsule is calculated to be about 5 M—this is 1,000 times the concentration of the reactants in the bulk solution (4 mM). Consistent with these estimates, the effective molarity[11] calculated from the rate data (k_{cat}/k_{uncat}) gives a value of 2.4 M for the encapsulated reactants.

The results here augur well for the application of reversibly formed molecular assemblies as reaction chambers. If the size and shape selectivity observed in their binding of ground states can be extended to preferential recognition of transition states[12,13] or even high-energy intermediates, then true catalysis via encapsulation could result. To release the product, it may be possible to use the approach devised by Hilvert[14] in antibody catalysis, which takes advantage of a subsequent reaction of the Diels–Alder product that alters its shape and affinity for the binding site and forces turnover. The general problem of product inhibition may be overcome in the future by using dissociative processes, reactions that result in an increased number of encapsulated species. At present, the evidence reported here indicates that in addition to heat, pressure, acids, antibodies[14], micelles[15–18], medium[19,20] and template effects[21], Diels–Alder reactions can also be promoted by reversible encapsulation. □

Received 14 August; accepted 31 October 1996.

1. Sherman, J. C. & Cram, D. J. *J. Am. Chem. Soc.* **117,** 4527–4528 (1989).
2. Garel, L., Dutasta, J.-P. & Collet, A. *Angew. Chem. Int. Edn Engl.* **32,** 1169–1171 (1993).
3. Cram, D. J., Tanner, M. E. & Thomas, R. *Angew. Chem. Int. Edn Engl.* **30,** 1024–1027 (1991).
4. Timmerman, P., Verboom, W., van Veggel, F. C. J. M., van Duynhoven J. P. M. & Reinhoudt, D. N. *Angew. Chem. Int. Edn Engl.* **33,** 2345–2348 (1994).
5. Wyler, R., de Mendoza, J. & Rebek, J. Jr *Angew. Chem. Int. Edn Engl.* **32,** 1699–1701 (1993).
6. Valdés, C., Spitz, U. P., Toledo, L., Kubik, S. & Rebek, J. Jr *J. Am. Chem. Soc.* **117,** 12733–12745 (1995).
7. Meissner, R. S., de Mendoza, J. & Rebek, J. Jr *Science* **270,** 1485–1488 (1995).
8. Kang, J. & Rebek, J. Jr *Nature* **382,** 239–241 (1996).
9. Kelly, T. R., Meghani, P. & Ekkundi, V. S. *Tetrahed. Lett.* **31,** 3381–3384 (1990).
10. Meissner, R., Garcias, X., Mecozzi, S. & Rebek, J. Jr *J. Am. Chem. Soc.* (in the press).
11. Kirby, A. J. *Adv. Phys. Org. Chem.* **17,** 183–278 (1980).
12. Mock, W. L., Irra, T. A., Wepsiec, J. P. & Adhya, M. *J. Org. Chem.* **54,** 5302–5308 (1989).
13. McCurdy, A., Jimenez, L., Stauffer, D. A. & Dougherty, D. A. *J. Am. Chem. Soc.* **114,** 10314–10321 (1992).
14. Hilvert, D., Hill, K. W. & Auditor, M. T. M. *J. Am. Chem. Soc.* **111,** 9261–9263 (1989).
15. Grieco, P. A., Garner, P. & He, Z.-M. *Tetrahedr. Lett.* **24,** 1897–1900 (1983).
16. Breslow, R., Maitra, U. & Rideout, D. *Tetrahedr. Lett.* **24,** 1901–1904 (1983).
17. Braun, R., Schuster, F. & Sauer, J. *Tetrahedr. Lett.* **27,** 1285–1288 (1986).
18. Singh, V. K., Raju, B. N. S. & Deota, P. T. *Synth. Commun.* **18,** 567–574 (1988).
19. Grieco, P. A., Kaufman, M. D., Daeuble, J. F. & Saito, N. *J. Am. Chem. Soc.* **118,** 2095–2096 (1996).
20. Breslow, R. & Guo, T. *J. Am. Chem. Soc.* **110,** 5613–5617 (1988).
21. Walter, C. J., Anderson, H. L. & Sanders, J. K. M. *J. Chem. Soc. Chem. Commun.* 459–460 (1993).
22. Mohamadi, F. *et al. J. Comput. Chem.* **11,** 440–467 (1990).

ACKNOWLEDGEMENTS. We thank J. Brauman, D. Hilvert, J. Stubbe, J. Williamson and M. Heagy for discussions. This work was supported by the National Institutes of Health.

CORRESPONDENCE should be addressed to J.R. at the Skaggs Institute for Chemical Biology (e-mail: jrebek@scripps.edu).

Infrared remote sensing of breaking waves

A. T. Jessup*, C. J. Zappa*, M. R. Loewen† & V. Hesany*

* Applied Physics Laboratory, University of Washington, Seattle, Washington 98195, USA
† Department of Mechanical and Industrial Engineering, University of Toronto, Toronto, Ontario, M5S 3G8, Canada

ENERGY dissipation due to deep-water wave breaking plays a critical role in the development and evolution of the ocean surface wave field. Furthermore, the energy lost by the wave field via the breaking process is a source for turbulent mixing and air entrainment, which enhance air–sea heat and gas transfer[1–3]. But the current lack of reliable methods for measuring energy dissipation associated with wave breaking inhibits the quantitative study of processes occurring at ocean surfaces, and represents a major impediment to the improvement of global wave-prediction models[4]. Here we present a method for remotely quantifying wave-breaking dynamics which uses an infrared imager to measure the temperature changes associated with the disruption and recovery of the surface thermal boundary layer (skin layer). Although our present results focus on quantifying energy dissipation—in particular, we show that the recovery rate of the skin layer in the wakes of breaking waves is correlated with the energy dissipation rate—future applications of this technique should help to elucidate the nature of important small-scale surface processes contributing to air–sea heat[5] and gas[6] flux, and lead to a fuller understanding of general ocean–atmosphere interactions.

Under most circumstances, a net upward heat flux from the ocean to the atmosphere occurs by molecular conduction through the skin layer at the ocean surface. As a result, the surface, or skin, temperature of the ocean is less than the bulk temperature immediately below by a few tenths of a degree Celsius[7,8]. An infrared radiometer measures only the skin temperature because the optical depth of the infrared radiation detected, about 10 μm, is much less than the thickness of the skin layer, of the order of 1 mm (refs 9–11). Our measurements confirm an early result[12] showing that when the cool skin layer is momentarily disrupted by a breaking wave, the skin temperature of the resulting turbulent wake is approximately equal to the bulk temperature. As the wake subsides, the skin layer recovers, and the skin temperature returns to its original, cooler value. Infrared measurements of breaking waves made in the surf zone[12] show a recovery time of the order of 10 s. We have found that the time needed for the skin layer to recover depends on the ambient heat flux[13] and, most significantly for quantifying wave breaking, on the strength of the event. Therefore, infrared measurements of the skin-layer recovery process should provide the capability to remotely monitor free-surface turbulence under conditions of constant heat flux or when the heat flux dependence is known.

Our measurements were made using an infrared imager which provides a time series of two-dimensional images of the skin temperature as inferred from the infrared radiance. Figure 1 shows a sequence of simultaneous video and infrared images of a breaking wave that was taken in the open ocean (time increases *a* to *d*). The first three video images show the breaking wave propagating from right to left as it evolves from a narrow, curved ridge to an actively breaking crest, or whitecap. The first three infrared images show features of increased temperature that clearly correspond to the whitecap, which can be up to 0.1 °C warmer than its wake. Part of the whitecap signature is probably an apparent temperature increase due to increased emissivity[14] associated with surface roughness and bubbles. Of primary interest here is the portion of the wake where the temperature changes are associated with the skin-layer disruption due to breaking-

generated turbulence. In the fourth infrared image, a roughly circular region of increased temperature extends significantly beyond the area covered by the whitecap and residual foam in the corresponding video image. The extent and location of this warm patch imply that it corresponds to the turbulent wake of the breaking wave.

The crest speed of a breaking wave has been suggested as a useful measure of its scale[15] and has been used as such in field measurements of the breaking process[16]. We have found that the time required for the skin layer within the wake to recover is proportional to the speed of the breaking crest. Faster-moving waves dissipate more energy and produce more turbulence, resulting in longer skin-layer recovery times. Figure 2*a* shows time series of the normalized skin temperature deviation, T_n, at a location within the turbulent wake for two breaking waves with different crest speeds, C_b, and correspondingly different recovery times, τ. The rapid increase in T_n due to the passage of the whitecap is followed by a gradual decrease which takes longer for the faster-moving wave. In Fig. 2*b*, τ is plotted versus C_b for 36 events observed during a 6-hour period of steady environmental conditions (see Fig. 2 legend for details). Although the results shown in Fig. 2*b* demonstrate that the recovery time is correlated with crest speed, this scaling alone is not sufficient to conclude that the skin-layer recovery process can be used to quantify the dynamics of wave breaking.

To link the skin-layer recovery directly to the energy loss due to wave breaking, we examine the correlation between a measure of the skin-layer recovery rate, R_l, and an estimate of the energy dissipation rate per unit area, E. From the time series of skin temperature within the wake, the recovery rate is estimated by $R_l = \Delta T/\tau$, where ΔT is the temperature deviation corresponding to the change in T_n from its maximum to a level of 0.3 (see Fig. 2*a*). A measure of R_l that is dimensionally consistent with E (W m^{-2}) is given by the rate of heat transfer per unit area required to re-establish the skin layer; we define this parameter as the restoring heat flux, $Q_r = (\rho c_p \delta)R_l$, where ρ is the density of water, c_p is the

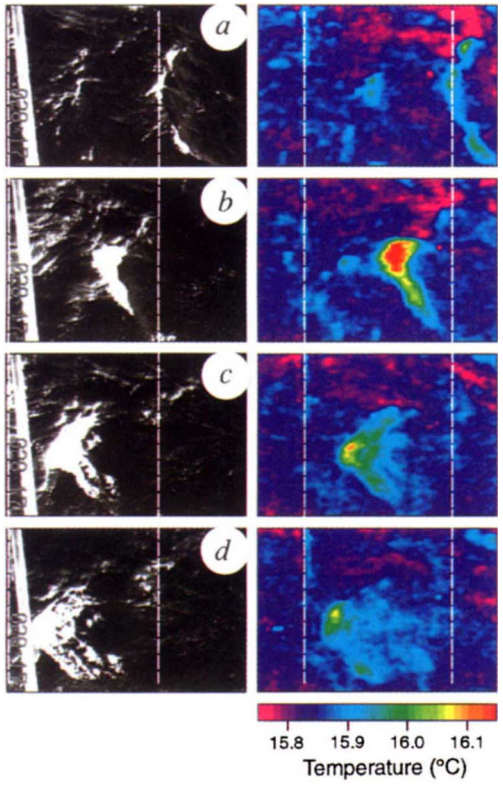

FIG. 1 Sequence of simultaneous, co-located video images (left) and infrared images (right) of a breaking wave in the open ocean. Image size is approximately 5 m × 10 m. The breaking wave is propagating from right to left; time increases down the page and spans 1.6 s. For reference purposes, each image includes two dashed vertical lines corresponding to roughly the same locations; the right-hand line denotes the leading edge of the breaking wave crest in the first frame. The whitecap in the video images appears as the warmest region in the infrared images. After the crest spills, a roughly circular warm patch remains (bottom-right image) which is significantly removed from the area dominated by the whitecap and foam. The infrared signature of the turbulent wake results from the disruption of the cool skin layer by the breaking wave. For this example, the bulk–skin temperature difference was ~0.15 °C and the wind speed was 7.7 m s^{-1}. The measurements were made using an infrared imager (Agema Model 880LW) operating at wavelengths of 8 to 12 μm aboard the research platform RP *FLIP* off San Diego, California. The temperature differences between the wake and undisturbed regions of the ocean surface that were derived from the infrared imagery were consistent with independent measurements of the bulk–skin temperature difference.

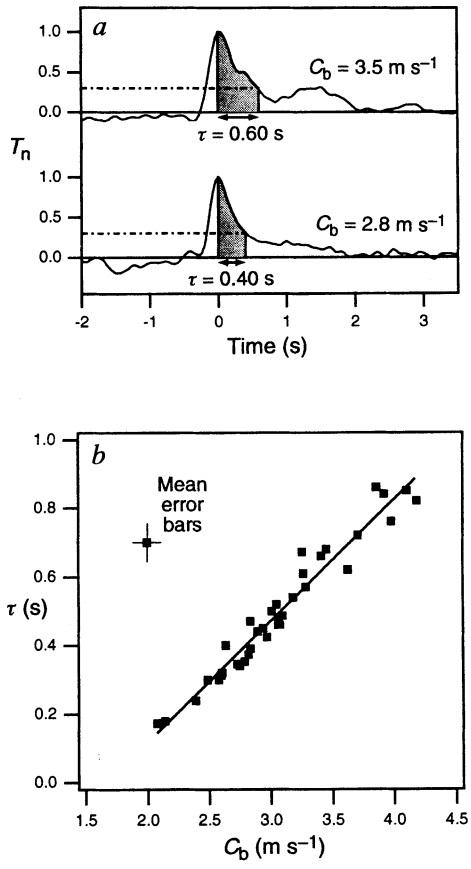

FIG. 2 *a*, Time series of T_n, the skin temperature deviation normalized by its maximum, for two oceanic breaking waves with different crest speeds, C_b, and skin-layer recovery times, τ. The skin temperature increases rapidly as the whitecap passes and then decays as the skin layer recovers. A three-step procedure was applied to infrared sequences like those in Fig. 1 to determine the crest length, crest speed, and recovery time. First, the area in each image was determined by applying a threshold of four standard deviations above the mean for the entire sequence. Second, the whitecap velocity and terminus were determined by tracking the centroid of the thresholded region. Last, a mean recovery time was computed for two regions measuring 0.5 m × 0.5 m and located ~0.5 m and 1.5 m behind the terminus and along the trajectory. The dashed line shows the T_n level of 0.3, which is used to define τ. This level of recovery was chosen to avoid uncertainty due to fluctuations sometimes observed after the initial recovery, such as the feature centred at ~1.5 s in the top trace. (These features suggest secondary turbulence sources, such as bubbles[2].) *b*, Plot of τ versus C_b for 36 oceanic breaking waves during steady conditions (the wind speed at 10 m was 7–8 m s^{-1} and the net ambient heat flux, Q_{net}, determined from bulk methods was 120–130 W m^{-2} upwards). The vertical error bars show the average range of τ values, and the horizontal error bars reflect the average accuracy of the linear regression used to determine the component white-cap velocities. The correlation coefficient for the linear fit shown is 0.975.

specific heat of water, and δ is the thermal boundary layer thickness (taken as 0.5 mm for the observed wind conditions[10,11]).

For an estimate of E, we use laboratory results showing that the rate of energy dissipation per unit crest length for quasi-steady[17] and unsteady[18] breaking waves is proportional to $\rho C^5/g$, where C is the breaking-wave phase speed and g is the gravitational acceleration. This relation has been employed in a number of recent efforts to model wave breaking in the open ocean[15,18,19]. The area over which the dissipation occurs corresponds to the spatial extent of the turbulent wake. Most of the infrared wake signatures we have observed are roughly circular (Fig. 1), which suggests that the wake's dimension in the direction of propagation may be approximated by the length of the breaking crest. This assumption is consistent with previous measurements of the ratio of the breaking-crest length to the distance of wave advance during breaking[2]. Therefore, an estimate of the energy dissipation rate per unit area is $E = 0.0032\,(\rho C_b^5/g)/L_b$, where L_b is the breaking-crest length and the proportionality constant is that for unsteady spilling breakers[18].

The variation of the skin-layer recovery rate with the energy dissipation rate is illustrated in Fig. 3 by plotting Q_r versus E. The restoring heat flux is correlated with the energy dissipation rate per unit area due to breaking. Note that Q_r is only part of the total breaking-induced heat flux as it does not include the contribution due to mixing below the skin layer. Furthermore, we estimate the effect of Q_r on the net ambient heat flux, Q_{net}, to be small because Q_r occurs only for the duration and over the extent of the breaking events, whereas Q_{net} is continuous in space and time. We emphasize that the utility of Q_r lies in its proportionality to the skin-layer recovery rate. Since Q_r is proportional to R_l, the results in Fig. 3 demonstrate that the skin-layer recovery rate in the wakes of breaking waves provides a measure of the energy dissipation rate due to breaking.

The field results are supported by complementary laboratory measurements of individual, mechanically generated breaking waves ranging in size from spilling to plunging. The technique we employed, in which the fraction of wave energy dissipated can be varied systematically, has been used extensively to investigate energy dissipation due to wave breaking[20–23]. In the absence of wind, experiments using this technique have shown that turbulent kinetic energy remains measurable for 30–60 wave periods after breaking[22]. Figure 4*a* shows examples of three laboratory time series of T_n for breaking waves in the absence of wind. For these measurements, Q_r was computed using the R_l value given by the slope of the temperature deviation over 30 wave periods (here δ is taken as 3 mm for no wind[24]). Figure 4*b* shows Q_r versus E for the laboratory measurements. As in the field, Q_r and E are correlated. The difference in the magnitude of Q_r between these results, measured in a laboratory without wind, and the field results shown in Fig. 3 is a manifestation of the additional dependence of the skin-layer recovery process on ambient conditions[13]. The wind-generating facilities available during the laboratory experiments reported here permitted us to examine only low wind-speed conditions. Nonetheless, Q_r for wind speeds from 2 to 3 m s^{-1} was $\sim$300 W m^{-2} (taking $\delta = 2$ mm for the given wind conditions[10,11]), which is in the range of field values shown in Fig. 3.

These field and laboratory results show that infrared measurements provide a means of remotely quantifying the dynamics of surface-wave breaking. The rate of the skin-layer recovery in the wakes produced by breaking waves is correlated with the rate of energy dissipation due to wave breaking. Airborne applications of

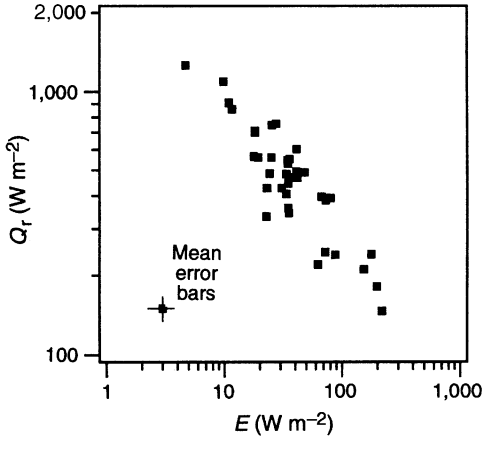

FIG. 3 The restoring heat flux, Q_r, versus the energy dissipation rate per unit area, E, for the oceanic breaking events shown in Fig. 2*b*. The correlation between Q_r and E implies that the skin-layer recovery rate, R_l, provides a measure of energy dissipation because Q_r is proportional to R_l. The error bars are analogous to those shown in Fig. 2*b*.

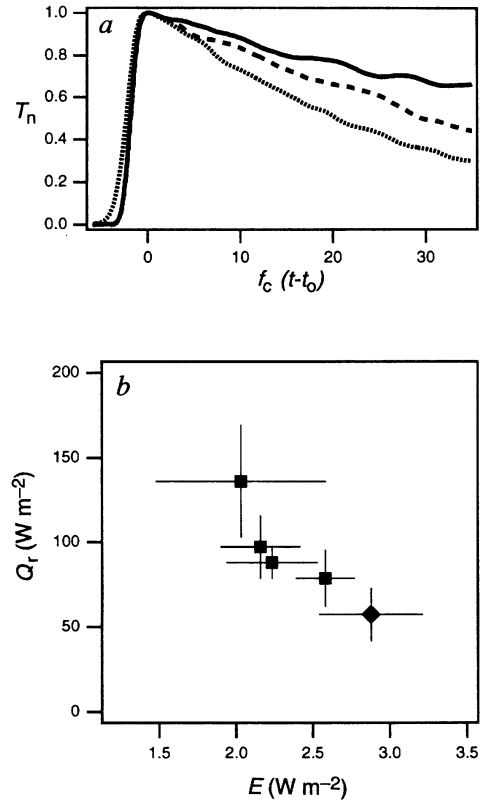

FIG. 4 *a*, Time series of T_n, the skin temperature deviation normalized by its maximum, for three laboratory breaking waves of different amplitude corresponding to a slope[22] of 0.24 (dotted line), 0.25 (dashed line) and 0.27 (solid line). The abscissa is time expressed in wave periods since breaking, where f_c is the centre frequency of the wave packet, t is time, and t_0 is the time of breaking onset. *b*, The restoring heat flux, Q_r, versus the energy dissipation rate per unit area, E, for breaking waves generated mechanically in the laboratory for constant air–water temperature difference and no wind. Each point is an ensemble average of five repetitions and the error bars represent one standard deviation. The squares denote single breaking events and the diamond a double breaking event. The experiments were conducted in a 10-m long, 30-cm wide, and 40-cm deep wave tank located at the Canada Centre for Inland Waters. Measurements were made of the water and air temperatures and surface displacement, and infrared images were recorded using the same imager as in the field experiments. Breaking waves were produced by programming a hydraulic wave-maker to focus a dispersive wave packet at a fixed distance down the tank. The wave packet was synthesized from 32 sinusoidal components and had a centre frequency of 1.12 Hz, corresponding to a wavelength of 1.2 m. The quantity E is given by $0.5\rho g C_g(\eta_0^2 - \eta_f^2)T_s/(Lt_b)$, where C_g is the group velocity of the centre component of the packet, η_0^2 and η_f^2 are the surface displacement variances upstream and downstream of breaking, respectively, and T_s is the sampling period for the displacement variance[23]. L is the along-tank length of the breaking region determined from the infrared images and t_b is the duration of the event as measured by a hydrophone.

this technique should provide remote measurements of energy dissipation due to wave breaking, which are necessary to improve wave prediction models used for operational sea-state forecasting. The capability to quantify the spatial and temporal characteristics of the skin-layer recovery has applications to other air–sea transfer processes that are directly affected by breaking-generated turbulence. Limitations in our understanding of ocean mixing and air–sea exchange mechanisms have hampered coupled models of the atmosphere and ocean used for global climate studies[25]. The fluxes of heat and gas across the air–sea interface are enhanced by the local increase in turbulence associated with wave breaking, and the skin-layer recovery rate has been shown to be directly related to properties of the free-surface turbulence. Furthermore, models of bubble-mediated gas transfer are critically dependent on accurate estimates of the surface area affected by wave breaking[26], which corresponds to the area of the detected wake. Although our results focus on remotely quantifying energy dissipation due to wave breaking, we conclude that infrared techniques may also lead to better predictions of air–sea heat and gas flux[27–29]. □

Received 5 December 1995; accepted 5 November 1996.

1. Banner, M. L. & Peregrine, D. H. *Annu. Rev. Fluid Mech.* **25,** 373–397 (1993).
2. Thorpe, S. A. *Prog. Oceanogr.* **35,** 315–352 (1995).
3. Melville, W. K. *Annu. Rev. Fluid Mech.* **28,** 279–321 (1996).
4. Komen, G. J. *et al. Dynamics and Modelling of Ocean Waves* (Cambridge Univ. Press, 1994).
5. Farmer, D. M. & Gemmrich, J. R. *J. Phys. Oceangr.* **26,** 816–825 (1996).
6. Kitaigorodskii, S. A. *J. Phys. Oceanogr.* **14,** 960–972 (1984).
7. Katsaros, K. B. *Boundary-Layer Meteorol.* **18,** 107–127 (1980).
8. Robinson, I. S., Wells, N. C. & Charnock, H. *Int. J. Remote Sens.* **5,** 19–45 (1984).
9. McAlister, E. D. & McLeish, W. *J. Geophys. Res.* **74,** 3408–3414 (1969).
10. Wu, J. *J. Phys. Oceanogr.* **1,** 284–286 (1971).
11. Hill, R. H. *J. Phys. Oceanogr.* **2,** 190–198 (1972).
12. Ewing, G. & McAlister, E. D. *Science* **131,** 1374–1376 (1960).
13. Jessup, A. T., Zappa, C. J., Hesany, V., Loewen, M. R. & Skafel, M. G. in *Air–Water Gas Transfer* (ed. Jähne, B. & Monahan, E. C.) 601–610 (AEON Verlag & Studio, Hanau, 1995).
14. Eisner, L., Bell, E. E., Young, J. & Oetjen, R. A. *J. Opt. Soc. Am.* **52,** 201–209 (1962).
15. Phillips, O. M. *J. Fluid Mech.* **156,** 505–531 (1985).
16. Ding, L. & Farmer, D. M. *J. Phys. Oceanogr.* **24,** 1368–1387 (1994).
17. Duncan, J. H. *Proc. R. Soc. Lond. A* **377,** 331–348 (1981).
18. Melville, W. K. *J. Phys. Oceangr.* **24,** 2041–2049 (1994).
19. Thorpe, S. A. *J. Phys. Oceanogr.* **23,** 2498–2502 (1993).
20. Chan, E. S. & Melville, W. K. *Proc. R. Soc. Lond. A* **417,** 95–131 (1988).
21. Melville, W. K. & Rapp, R. J. *Nature* **317,** 514–516 (1985).
22. Rapp, R. J. & Melville, W. K. *Phil. Trans. R. Soc. Lond. A* **331,** 735–800 (1990).
23. Loewen, M. R. & Melville, W. K. *J. Fluid Mech.* **224,** 601–623 (1991).
24. Katsaros, K. B., Liu, W. T., Businger, J. A. & Tillman, J. E. *J. Fluid Mech.* **83,** 311–335 (1977).
25. Barron, E. J. *Eos* **76,** 185–190 (1995).
26. Keeling, R. F. *J. Mar. Res.* **51,** 237–271 (1993).
27. Jähne, B., Libner, P., Fischer, R., Billen, T. & Plate, E. J. *Tellus* **41B,** 177–195 (1989).
28. Soloviev, A. V. & Schlüssel, P. *J. Phys. Oceanogr.* **24,** 1339–1346 (1994).
29. Haußecker, H. & Jähne, B. in *Air–Water Gas Transfer* (eds Jähne, B. & Monahan, E. C.) 775–784 (AEON Verlag & Studio, Hanau, 1995).

ACKNOWLEDGEMENTS. We thank the crew of RP *FLIP* and our colleagues at the University of Washington for their field assistance; M. G. Skafel, D. Doede (National Water Research Institute, Environment Canada) and M. A. O'Dor for their laboratory assistance; and F. Herr (ONR) for his early support and encouragement. This work was supported by the Applied Physics Laboratory, ONR, and NASA. M.R.L. was supported by a grant from the Natural Sciences and Engineering Research Council of Canada.

CORRESPONDENCE should be addressed to A.T.J. (e-mail: jessup@apl.washington.edu).

Emplacement of a large igneous province as a possible cause of banded iron formation 2.45 billion years ago

M. E. Barley*, A. L. Pickard* & P. J. Sylvester†

* Key Centre for Strategic Mineral Deposits, The University of Western Australia, Nedlands WA 6907, Australia
† Research School of Earth Sciences, The Australian National University, Canberra, ACT 0200, Australia

LATEST **Archaean and earliest Palaeoproterozoic times (from 2.6 to 2.2 billion years ago) have generally been viewed as a largely quiescent period of Earth history; the geological record indicates the very slow deposition of pelagic and chemical sediments[1,2], and bears only a limited record of magmatic and tectonic activity[3–5]. Such quiescence is consistent with the contention that the Earth's main banded iron formations (BIFs)—finely laminated chemical sedimentary rocks, rich in iron oxide—formed slowly as oxygen abundances in the oceans gradually increased, thus reducing the capacity of sea water to retain dissolved iron[6–10]. Here we show that a large igneous province, comprising >30,000 km^3 of dolerite, basalt and rhyolite, accompanied deposition of a Hamersley Province BIF 2,449 ± 3 million years ago. This observation indicates that Hamersley BIFs formed during a major tectono-magmatic event and were deposited very much faster than previously thought, at similar rates to (or faster than) modern pelagic sediments. Thus the largest Palaeoproterozoic BIFs, rather than simply reflecting a gradual increase in the oxygen content of the oceans during a period of tectonic quiescence, are more likely to have formed as a result of an increased supply of suboxic iron- and silica-rich sea water upwelling onto continental shelves during a pulse (or pulses) of increased submarine magmatic and hydrothermal activity.**

Palaeoproterozoic BIFs are both a very significant indicator of Precambrian environmental conditions and the most important source of iron ores. The BIFs of the Hamersley Province in northwestern Australia, which form part of the 2.77–2.41-Gyr Mount Bruce Megasequence Set, are the world's thickest and most extensive (>50,000 km^2) deposits of this type[11,12]. They are finely laminated, chemical sedimentary rocks composed largely of microcrystalline quartz (chert) and iron oxide, with no modern counterparts. As a result, both their origin and tectonic context have been interpreted previously in nonuniformitarian terms as a conformable succession of rock units that formed continuously in a slowly subsiding intracratonic basin, continental shelf or submarine plateau, starved of clastic sediment and with little magmatic activity[12,13]. The origin of iron and silica in such extensive finely laminated rocks is problematical and requires either that there was a direct magmatic-hydrothermal input to depositional basins[14–17], or that continuously upwelling iron-rich waters from suboxic marine basins encountered more oxygen-rich waters on continental shelves[6–8,17]. Iron oxides were simultaneously precipitated over large areas when a threshold oxygen activity was reached, perhaps as seasonal deposits in response to activity in the biosphere[6,8,17,18]. The apparent absence of magmatic activity during deposition of the Hamersley BIFs is a key factor in the latter model and in arguments that Palaeoproterozoic BIFs reflect a gradual transition from suboxic to oxic conditions in the hydrosphere, rather than periods of enhanced magmatic and hydrothermal activity in marine basins[6–10].

The oldest rocks in the Hamersley Province are flood basalts, rhyolites and fluvial, lacustrine and marine clastic sedimentary rocks of the 2.77–2.6-Gyr Chichester Range Megasequence (Fig. 1), which formed before, and during, the breakup and dispersal of a Late Archaean continent[11]. These are overlain by the 2.6–2.41-Gyr Hamersley Range Megasequence. Initial deposition of BIFs, turbidites, organic and pyritic shales and carbonate sedimentary rocks (the Marra Mamba Supersequence Package) occurred on a continental shelf[13]. The Brockman Supersequence Package is dominated by BIFs with a cumulative thickness of >500 m with lesser fine tuff, turbidites, organic and pyritic shales, dolomite and